Melt layer motion and droplet ejection under divertor-relevant plasma conditions

G. De Temmerman[1], J. Daniels[1], K. Bystrov[1], M.A. van den Berg[1], and J.J. Zielinski[1]

[1]FOM Institute DIFFER, Dutch Institute For Fundamental Energy Research, Edisonbaan 14, 3439 MN Nieuwegein, The Netherlands

E-mail: `g.c.detemmerman@differ.nl`

Abstract.

Accidental melting of metallic plasma-facing materials in future fusion devices poses serious issues regarding the material lifetime and power-handling capabilities as well as core plasma performances. The behaviour of aluminum (as a proxy for beryllium) and tungsten materials has been investigated in the Pilot-PSI linear plasma device to study the melt layer motion and droplet ejection under ITER-relevant plasma conditions. Heat fluxes of up to 50 MW·m^{-2} raised the surface temperature to values up to 5000 K. The melt layer rotation was found to depend on the magnetic field (up to 1.6 T) strength and target potential and is attributed to J × B forces caused by radial currents in the plasma. The amount of droplets ejected from the molten surface depends on the material- more droplets ejected from aluminum than from tungsten- and the heat flux to the target. The average droplet velocity was determined to be around 60 m·s^{-1} for both materials with droplets being ejected mainly in the axial direction. Droplet ejection is only observed during helium discharges, no ejection can be observed with hydrogen plasmas despite similar heat fluxes. Bubble boiling appears to be the main mechanism contributing to the observed droplet ejection.

PACS numbers: 52.40.Hf, 52.55Rk, 52.77.Dq

1. Introduction

Tungsten is currently the material of choice as a divertor material for ITER [1] and future fusion devices, owing to its low sputtering yields, high thermal conductivity and high melting point. In addition, tungsten presents the advantage of a low tritium retention both by implantation [2] and co-deposition [3, 4]. Contrary to CFC however, tungsten can melt under the excessive heat loads which can happen either during loss of detachment or transient events such as disruptions and Edge-Localized Modes (ELMs) [1, 5]. The occurence of melting has two immediate, and negative, consequences. First, this can represent a large source of high-Z impurities in the core plasma and second it will modify the plasma-facing material geometry and power handling capabilities.

Dedicated experiments have been carried out in tokamaks [6, 7], electron and plasma guns [8, 9, 10] and have shown the existence of significant melt layer motion and droplet ejection during melting. Characterization of the droplet ejection has been carried out but in those experiments was limited by diagnostic in tokamaks and by the non-relevant plasma conditions in the plasma gun facilities. The impact of the ejected droplets on the plasma performances will depend on their ability to reach the core plasma. In the case of dust particles for example, it has been shown that this will depend critically on the dust particle material, size and initial velocity [11, 12], which in turn will depend on the droplet creation mechanism. The latter will depend on the plasma conditions in front of the plasma-facing surface, which for the ITER divertor cannot be matched in existing tokamaks. The condequences of melting and droplet ejection from molten surfaces have been observed, for example, in Alcator C-Mod, where H-mode operation was impossible [13]. Similarly, a strong increase in the radiated power could be correlated with the penetration of large tungsten droplets in the plasma core of TEXTOR [6].

Experiments were performed under high-density plasma conditions, similar to those expected in the ITER divertor, in the Pilot-PSI linear plasma device to study the melting of aluminum (as a proxy for beryllium) and tungsten. The use of aluminum is mainly aimed at characterizing the droplet ejection and melt layer motion of a metal with a lower melting point than tungsten. Taking advantage of the good diagnostic and surface access, the emphasis was put on the study of droplet ejection and the characterization of their main properties such as velocity and angular distribution.

2. Experimental

Experiments were carried out in the Pilot-PSI linear plasma generator (fig. 1). The plasma is generated by a so-called cascaded arc source and exhausts into the vacuum vessel. An axial magnetic field (0.4-1.6T) is used to confine the plasma and generate an intense magnetized cylindrical plasma beam. In addition, the device offers the unique possibility to combine the continuous plasma with a transient heat and particle pulse (up to 1.2 GW·m^{-2} for 1 ms) allowing the study of ELM effects on plasma-exposed surfaces [14].

Tungsten and aluminum samples were mounted on the water-cooled cooling system. The tungsten material used in this study was rolled tungsten from Plansee, and had a purity of 99.97%. The aluminum samples were cut from a rod of as-drawn aluminum with a purituy of 99.999%. In the case of tungsten, a stack of four tungsten discs was used to minimize the amount of cooling to the plasma-facing surface making it easier to reach the necessary high temperatures. The discs had a diameter of 30 mm and a thickness of 1 mm. No special surface preparation (such as polishing) was used in this study. The aluminum samples had a similar diameter but a single disc, 4 mm thick, was used.
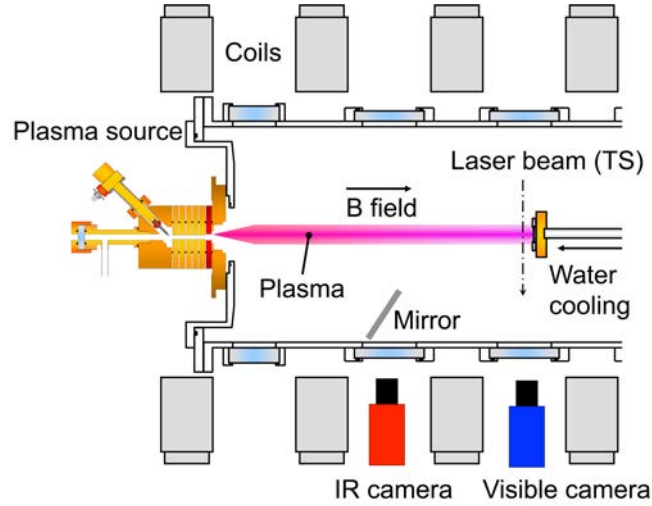

Figure 1. Schematic view of the Pilot-PSI linear plasma generator illustrating the arrangement of the diagnostics used during the melting experiments.

The plasma parameters are measured by means of a Thomson scattering system [15] located 17 mm in front of the plasma exposed target (fig. 1). During plasma exposure, the surface temperature was measured by a fast infrared camera (FLIR SC7500MB) which measures infrared radiation in the wavelength range 2-5 μm. The frame rate of the camera was set to 1 kHz. The temperature-dependence of the surface emissivity is taken into account in the case of tungsten following the work by Sergienko [16] and Roberts [17]. Ejection of droplets from the melted surface during plasma exposure was monitored by a fast visible camera (Phantom v12) with a framerate of 15 kHz. Tangential observation was used to minimize the disturbances from the target infrared emission.

Both helium and hydrogen plasmas were used to study the possible role of the gas species on the observed droplet ejection. The magnetic field was varied in the range 0.8-1.6 T by steps of 0.4 T. The plasma parameters varied in the range $5\text{-}17\times10^{20}m^{-3}$ and 1-3 eV, respectively. The plasma beam has a gaussian profile with a full width at half maximum (FWHM) of about 10 mm. The resulting heat flux profile on the target is shown in fig. 2 for the highest achieved powers. The peak heat flux to the target is about 50 MW·m^{-2} in this case. For comparison, the steady-state peak heat
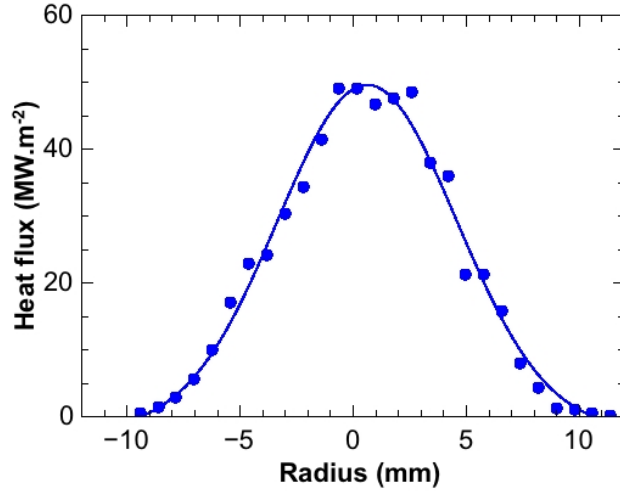
Figure 2. Example of the heat flux profile (derived from Thomson scattering measurements) during a helium discharge with a magnetic field of 1.6 T and a source current of 220 A. The peak value is close to 50 MW·m^{-2}.

flux in the ITER divertor is expected to be about 10 MW·m^{-2}, with possible slow transient events (loss of detachment for example) where this value could be increased to 20 MW·m^{-2} for a few seconds [18]. The peak heat flux in this study is thus representative of what would happen in case of the appearance of leading edges in the divertor. The maximum pulse duration depends on the magnetic field strength and varied between 10 and 40 s, with melting typically occuring within the first few seconds of exposure. In order to investigate the role of currents on the melt layer motion, the samples were either grounded, floating, or negatively biased (-40 V). In case of a grounded or biased target, the current through the target is measured.

3. Melt layer motion

Fig. 3 shows a sequence of infrared images from a tungsten surface in the melting phase. Melting is visible about 0.8 s after the beginning of the plasma exposure and the molten area can clearly be seen at 1.2 s (inside the dotted circle in fig. 3). As the plasma exposure goes on, both a radial expansion and a strong rotation of the molten material can be observed. The rotation induces instabilities in the liquid metal as can be observed from the surface ripples and their evolution at t=3.7 s and t=5.2 s.

The evolution of the surface temperature profile along a segment is shown in fig. 4. Until the onset of melting, the surface temperature profile depicts a gaussian shape in agreement with the heat flux profile shown in fig. 2. Once the melting has started, the surface temperature profile becomes hollow with the maximum temperature occuring away from the region of highest heat flux. Furthermore, the region of highest temperature moves radially outwards leaving a lower temperature in the middle. As mentioned earlier, the variation of the surface emissivity with temperature is taken into
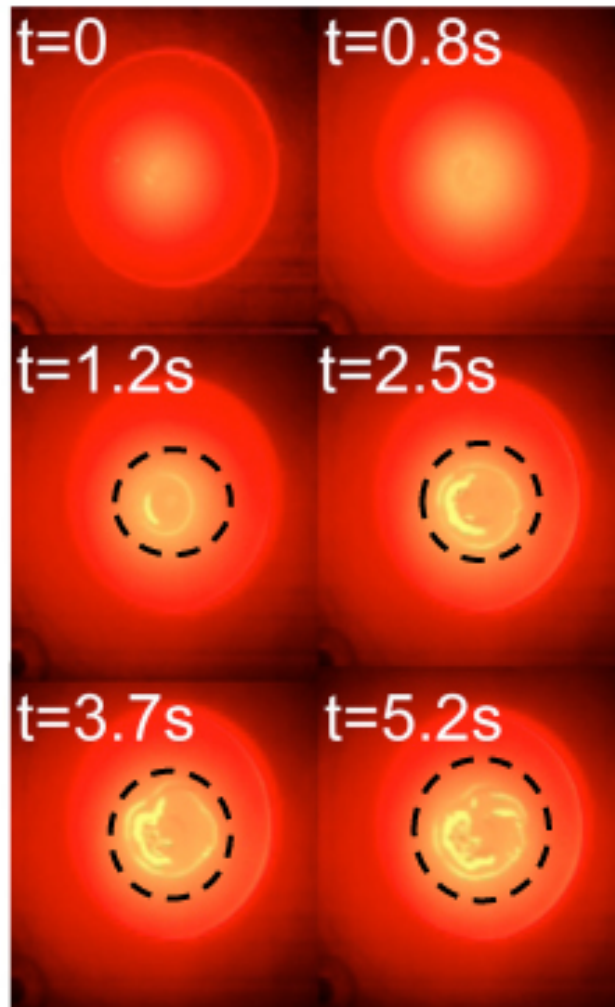
Figure 3. Sequence of infrared images (false colours) illustrating the evolution of the tungsten surface during melting. The target was kept at floating potential during this experiment and the magnetic field was 0.8 T.

account in the results presented here. Combining those observations with those made for fig. 3 indicates that there is indeed a net motion of liquid metal outwards. This is also confirmed by the common observation of a hole forming in the target centre after plasma exposure and accumulation of re-solidified material around the hole. The hollow temperature profile could be caused by vapour shielding [19] which is then less efficient at the edge of the plasma beam where the plasma density and temperature are lower. On the other hand, the heat flux gradient across the surface causes outward motion of the liquid metal through the so-called Thermo-Electric MHD effect [?] effectively cooling the target centre.

Another effect observed during the melting of tungsten is the occurrence of rotation of the melt layer under specific conditions. Due to limited contrast in the IR images in the hot melted areas of the sample, the only way the rotating melt could really
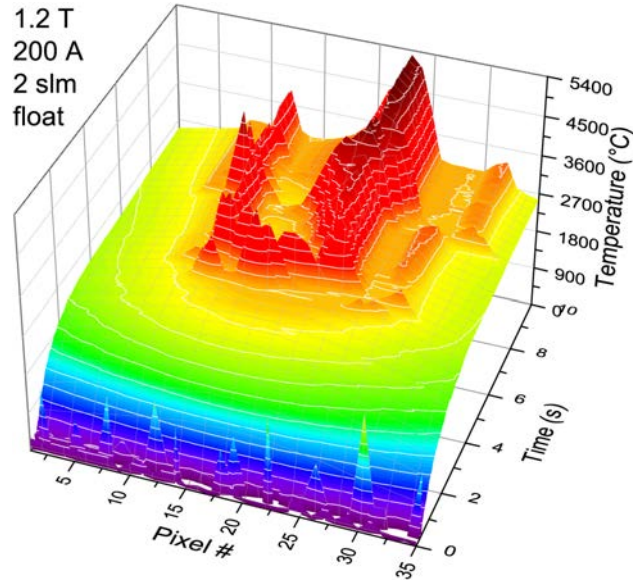
Figure 4. Temporal evolution of the surface temperature profile during melting of tungsten (B=1.2 T, floating target).

be observed is whenever a small bubble or excursion appeared, as shown in fig. 3. A typical property of the melt rotation is its frequency. It should be noted that at certain moments during the exposure, the melt displays varying rotational speeds at different positions. In those cases the clearest rotation was recorded. The evolution of the rotation frequency during plasma exposure is shown in fig. 5 for both tungsten and aluminium targets.

In most cases, a decrease of the rotation frequency is observed during the plasma exposure. For tungsten, rotation frequencies in the range 30-60 Hz are observed. The rotation frequency shows a light dependence on the magnetic field especially considering the difference between the cases at 1.2 T and 1.6 T in fig. 5a. An other indirect confirmation of this dependence appears when considering that the magnetic field decreases continuously during the plasma exposure, due to heating up of the coils. For the exposure made with B=1.2T and a source current of 220 A, the rotation frequency decreases by about 17% over the 5.5 s shown in fig. 5a while the magnetic field decreases by about 5%.

The most likely cause of the melt layer rotation seems to be a J × B force caused by currents in the sample and the main magnetic field. This explains the suggested dependence of the rotation on the magnetic field. The existence of such a force on a high B-field plasma interface has been confirmed in both experiment and simulation on the TEXTOR tokamak [21], albeit in a geometry different to that in Pilot-PSI. Other examples include the lithium divertor experiments on tokamak DIII-D [22] where J×B forces induce movement in a liquid lithium layer.

In Pilot-PSI, the thermoelectric current generated at high surface temperature is parallel to the magnetic field and so can not account for any melt layer motion, in
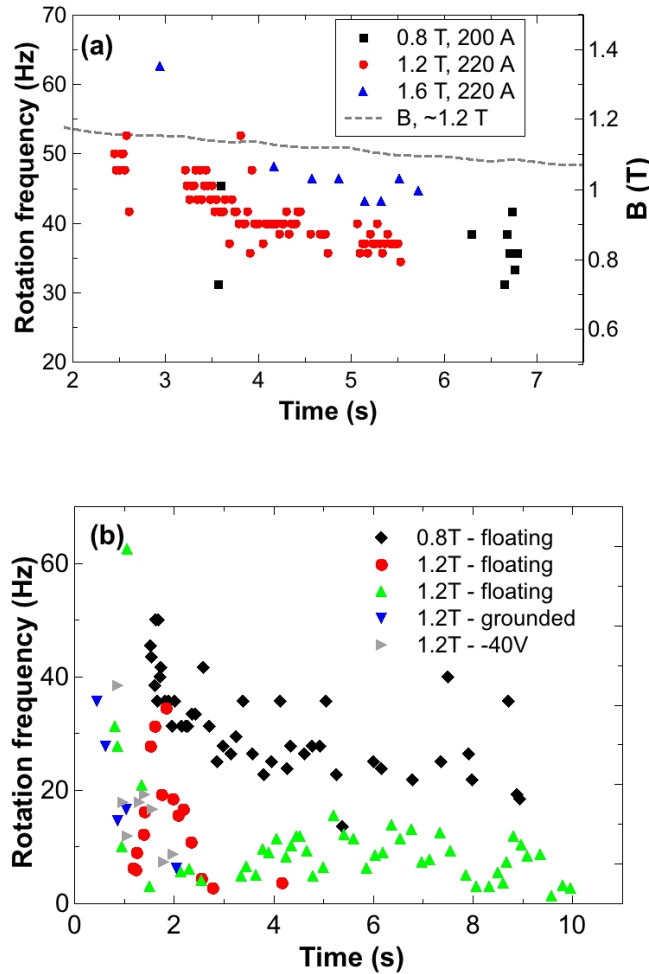
Figure 5. Temporal evolution of the melt layer rotation frequency for (a) tungsten and (b) aluminum targets for different conditions of magnetic field and electric potential. For (b) two individual datasets measured under otherwise identical conditions (1.2 T, floating) to illustrate the repeatability.

contrast with observations from TEXTOR. So where does the current that causes the J × B force come from? To begin with, a potential drop is created between the cathode and anode of the source to generate the plasma. In the presence of a strong magnetic field, the electron conductivity is much higher in the direction parallel to the magnetic field than in the direction perpendicular. The electrons cannot close the circuit within the source anymore and the radial electron current spreads out in the axial direction until the resistance of the axial and radial current paths are equal [23]. At high field, the electrically conducting target will serve as a short circuit for the electron current and a radial current through the target will exist which is then perpendicular to the magnetic field. The resulting J × B force will then act on the liquid metal and induce a rotation around the magnetic field direction. Since the radial current is caused by the magnetic confinement, a decrease of the magnetic field will also cause a decrease of the

radial current which would explain the decrease in the rotation frequency described in fig. 5a.

Fig. 5b illustrates the evolution of the melt layer rotation for aluminium targets under different conditions of magnetic field and target potential. As in the case of tungsten, a decrease of the rotation frequency is observed with time during the plasma exposure. No clear correlation between the magnetic field strength and the melt layer rotation frequency can be observed. However, it is important to mention that an increase of the magnetic field also increases the heat flux to the targets and that melting is very severe for aluminium since its melting temperature is relatively low. This leads to the rapid formation of a hole in the target at high fields, restricting the observation of melt layer rotation to areas well outside the region of highest heat fluxes. In this sense, the results described for aluminum are not necessarily contradicting the previously described observations made in the case of tungsten. When a potential is applied to the target, i.e. when it is not electrically floating, rotation is only observed at the very beginning of the melting phase and then cannot be observed anymore. Instead, a radial expansion of the liquid metal is observed. Considering the previous discussion about the origin of the melt layer rotation (J × B forces), the application of a potential to the sample means that some of the current is now allowed to flow through the sample changing the repartition of currents in the plasma beam. In the case of the grounded target for example, since the plasma potential is negative in Pilot-PSI, part of the electron current will flow through the target and not return to the anode, which decreases the perpendicular current and associated J × B force.

4. Droplet ejection

During the melting experiments, for both tungsten and aluminium targets, ejection of droplets was regularly observed using a fast visible camera. An example of this is shown in fig. 6. In order to study the droplet ejection in a quantitative fashion and follow the droplet trajectory and velocity, an algorithm was developed to detect droplets emitted from the melting surface (fig. 7). In essence, the algorithm is similar to that described in [24]. To check that the obtained results were reasonable, a reduced dataset was processed by manual detection of the particles. Both techniques yielded similar results.

The first noticeable thing in fig. 7 is the fact that independently of the target material and biasing conditions, droplet ejection is never observed after 1.6 s into the discharge. The grounded samples seem to start ejecting droplets earlier and also stop somewhat earlier, while the biased targets apparently eject at a later time. This is likely to be related to the fact that the surface temperatures in the grounded setup rise faster and melting occurs quicker, allowing for earlier ejection. In addition, large differences are observed in the numbers of detected droplet between the different materials and exposure conditions, even though all analysis parameters set in the detection routine were similar. Fig. 7 shows that the biased setup caused more droplets to be ejected per unit time, while less than average events were observed in the grounded setup. In
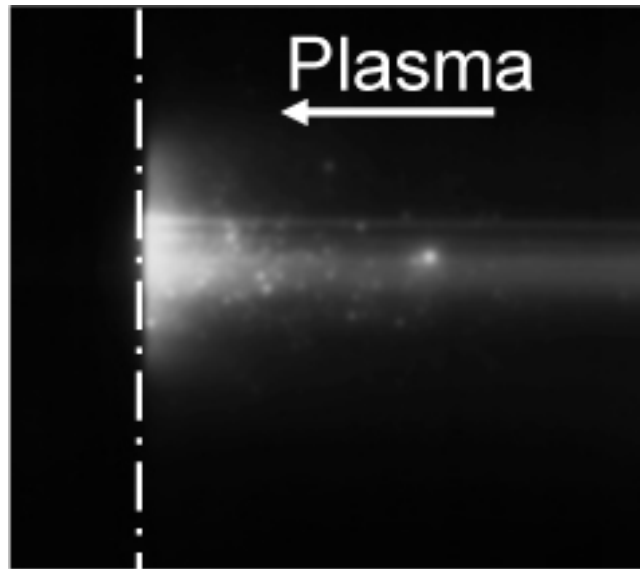
Figure 6. Fast camera image illustrating the ejection of droplets from the molten material during plasma exposure.
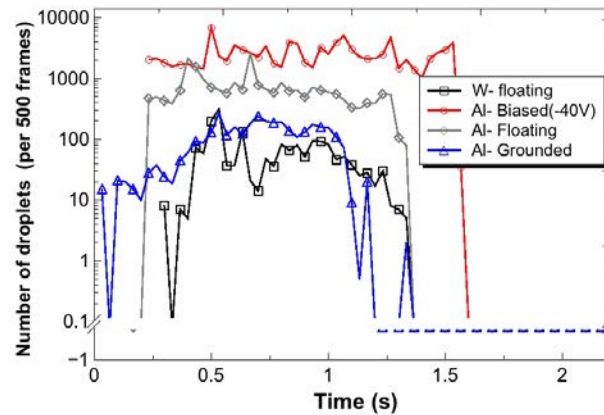

Figure 7. Number of droplets ejected from the liquid metal (per 500 camera frames or 33 ms) for different exposure conditions of aluminum and tungsten targets. The values are averaged over several experiments with identical parameters.

addition, comparatively much less droplets are observed to be ejected from the tungsten surface while again no droplet is observed to be ejected from the surface after around 1.4 s into the discharge.

Fig. 8 shows a statistical analysis of the droplet ejectrion angle, velocity and ejection location for tungsten targets. The angular distribution of the ejected droplets (fig. 8a) shows that the droplets are mainly ejected axially with a minimal amount of droplets being ejected at extreme angles. The angular distribution peaks in the direction parallel to the main magnetic field. A slight asymmetry is however observed with more particles being ejected with negative angles i.e. in the downward direction. This might be the
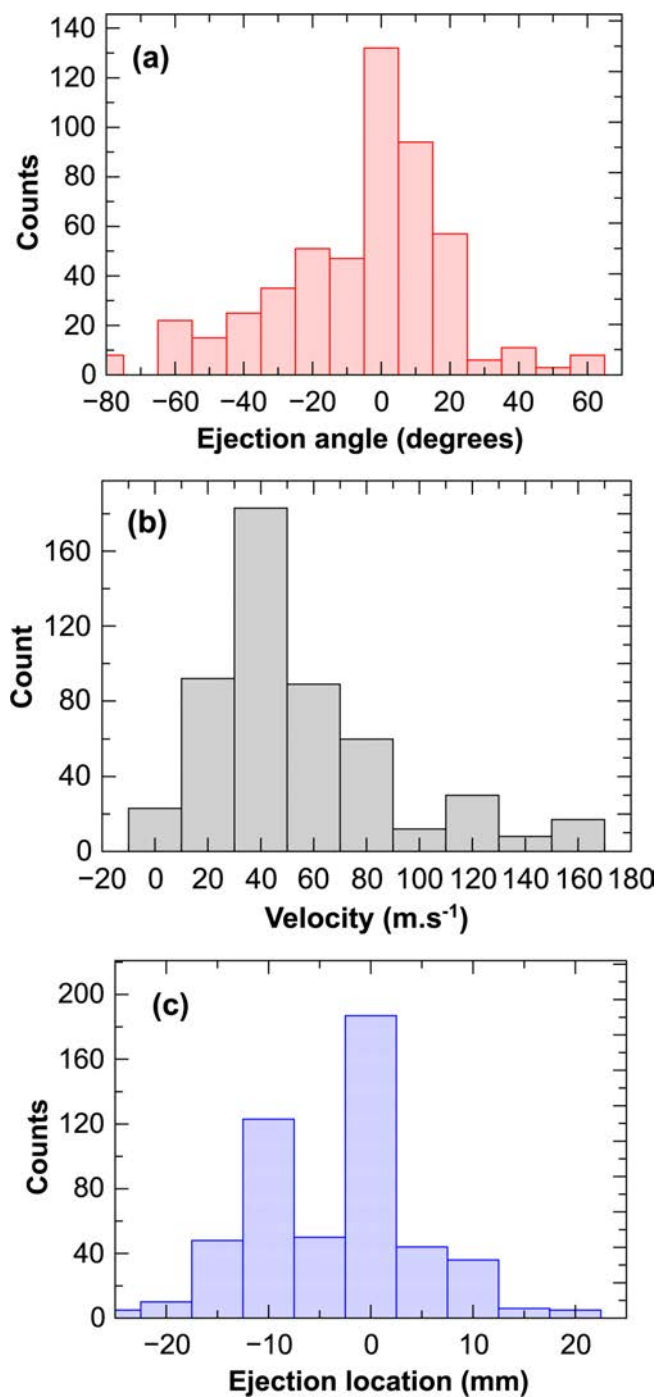
Figure 8. Statistical analysis of (a) the angular distribution, (b) the measured velocity and (c) ejection location of droplets ejected from a tungsten target.

influence of the gravity. However, all droplets necessarily have an initial axial velocity since no purely vertical motion is observed. The velocity distribution peaks at a value of 40 m·s^{-1}, while particle velocities as high as 160 m·s^{-1} can be observed. Most of the droplets seem to originate from the middle of the sample (fig. 8c) i.e. from the region exposed to the highest heat flux, although droplets can be observed originating

from everywhere on the surface. A similar analysis has been carried out in the case of aluminum targets. The angular distribution of the ejected droplet (fig. 9a) is relatively similar to that obtained for tungsten although the asymmetry is less pronounced. The velocity distribution ((fig. 9b) however peaks at velocities of 10-20 m·s^{-1} with most particles having velocities lower than 50 m·s^{-1}. The average velocity of aluminium droplet is about 58 m·s^{-1} but velocities as high as 270 m·s^{-1} have been measured.
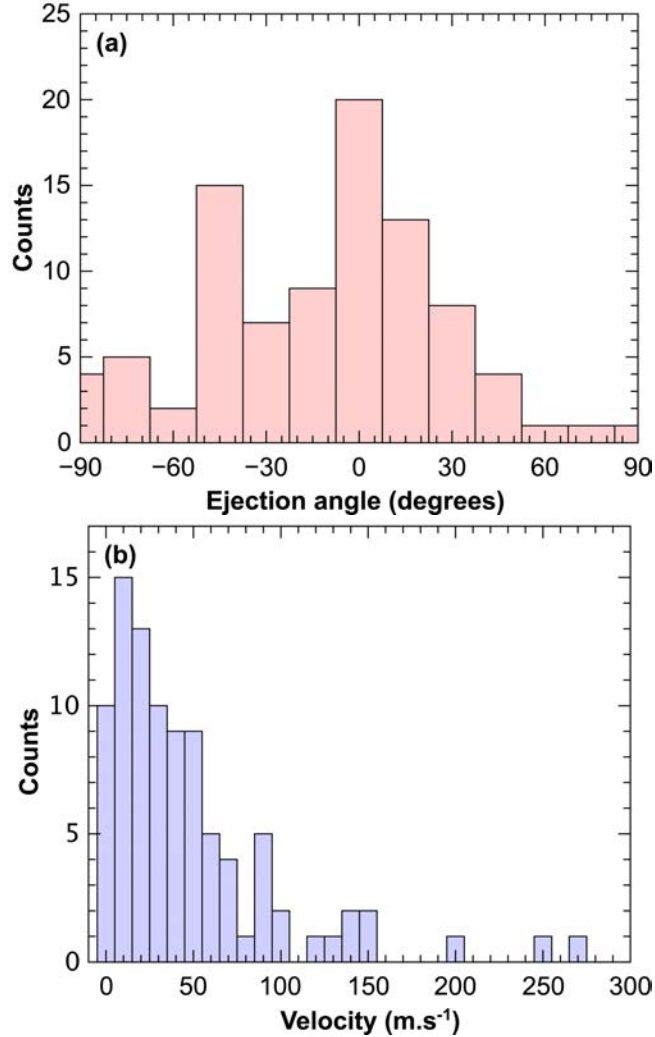

Figure 9. Statistical analysis of (a) the angular distribution and (b) the measured velocity of droplets ejected from an aluminum target.

Droplet ejection was observed in previous experiments done in tokamaks [6, 7] and powerful plasma guns [8, 9]. Two main mechanisms were proposed to explain the formation and ejection of liquid droplets from the melting material: Kelvin-Helmholtz instabilities [25, 26] and boiling-induced events [27]. Under the plasma conditions used in this study ($n_e \sim 10^{20}$-10^{21}m^{-3} and $v_{rot} \sim 1$-10×10^3m·s^{-1}), Kelvin-Helmholtz instabilities are expected not to play a significant role [26]. Droplet ejection by bubble boiling is the other candidate. Bubbles can form in the material by heterogeneous nucleation at

impurities, grain boundaries and defects such as voids, cracks, etc. [27]. Simulations [27] have shown that liquid metal droplets ejected by boiling can reach velocities of up to 60 m·s^{-1} and 90 m·s^{-1} for tungsten and aluminum droplets respectively for a 100 μm bubble radius, with lower bubble radii giving rise to faster droplets. Those values are consistent with the observed droplet velocities in Pilot-PSI and bubble boiling could explain the effects described in this article. The reason for droplet ejection to stop abruptly after 1.5-2s could be the intense vaporization occuring in front of the target and associated vapour shielding which would reduce the effective heat flux to the surface [19]. For aluminum, the maximum temperature is indeed reached after about 1-1.5 s, while this is reached after about 1.5-2s in the case of tungsten.

All the droplet ejections discussed so far were observed during exposures to pure helium plasmas. In linear devices such as Pilot-PSI, operations in pure helium allows for the highest heat fluxes since helium does not suffer from Molecular Assisted Recombination [28], unlike hydrogen, while its low mass allows for high velocities and hence particle fluxes to the surface. Experiments were also performed with pure hydrogen plasmas as the divertor plasma in a fusion reactior will be mainly composed of hydrogen isotopes. In order to obtain similar heat fluxes in both cases (and hence surface temperatures), the machine had to be operated at higher magnetic field and discharge currents in the case of hydrogen: 1.6 T and 220 A versus 1.2 T and 200 A. This might introduce some differences in terms of melt layer rotation (as describe above) which are deemed negligible in view of the obtained results. Fig. 10 shows a comparison of the fast camera observations and evolution of the surface temperature profiles during the matching helium and hydrogen discharges. In the hydrogen case, the background emission from the plasma is more pronounced (recall that the camera was not equipped with filters) but no droplet ejection can be observed throughout the discharge. Even if one assumes that this background emission might prevent the observation of some droplets, the measured ejection angle discussed previously imply that droplets should be observed outside of the plasma beam, which is not the case. Repeat of the experiments with other targets gave similar results. While the temperature profiles are slightly different for helium and hydrogen discharges, temperatures above 4000°C are obtained in both cases. Droplet ejection was observed to start when the temperature was between 3000 and 4000°C so that the discrepancies in temperature profile cannot account for the absence of droplet ejection in hydrogen. Melt layer rotation was observed during the hydrogen discharges with a typical rotation frequency between 35 and 50 Hz, comparing very well with that observed during helium-induced melting experiments.

The different behaviour observed for helium and hydrogen plasmas still needs to be clarified. It is well known that helium-irradiation of tungsten surfaces at elevated temperatures lead to the formation of voids. It has indeed been shown that voids with diameter up to 100-150 nm can be formed within 10 s of plasma exposure in Pilot-PSI at a surface temperature of 2000 ^{o}C [29]. Before melting, the tungsten samples are exposed to about 2 s of high flux helium plasma irradiation. Since the bubble boiling mechanism relies on bubble formation at defects such as voids, one could hypothesize
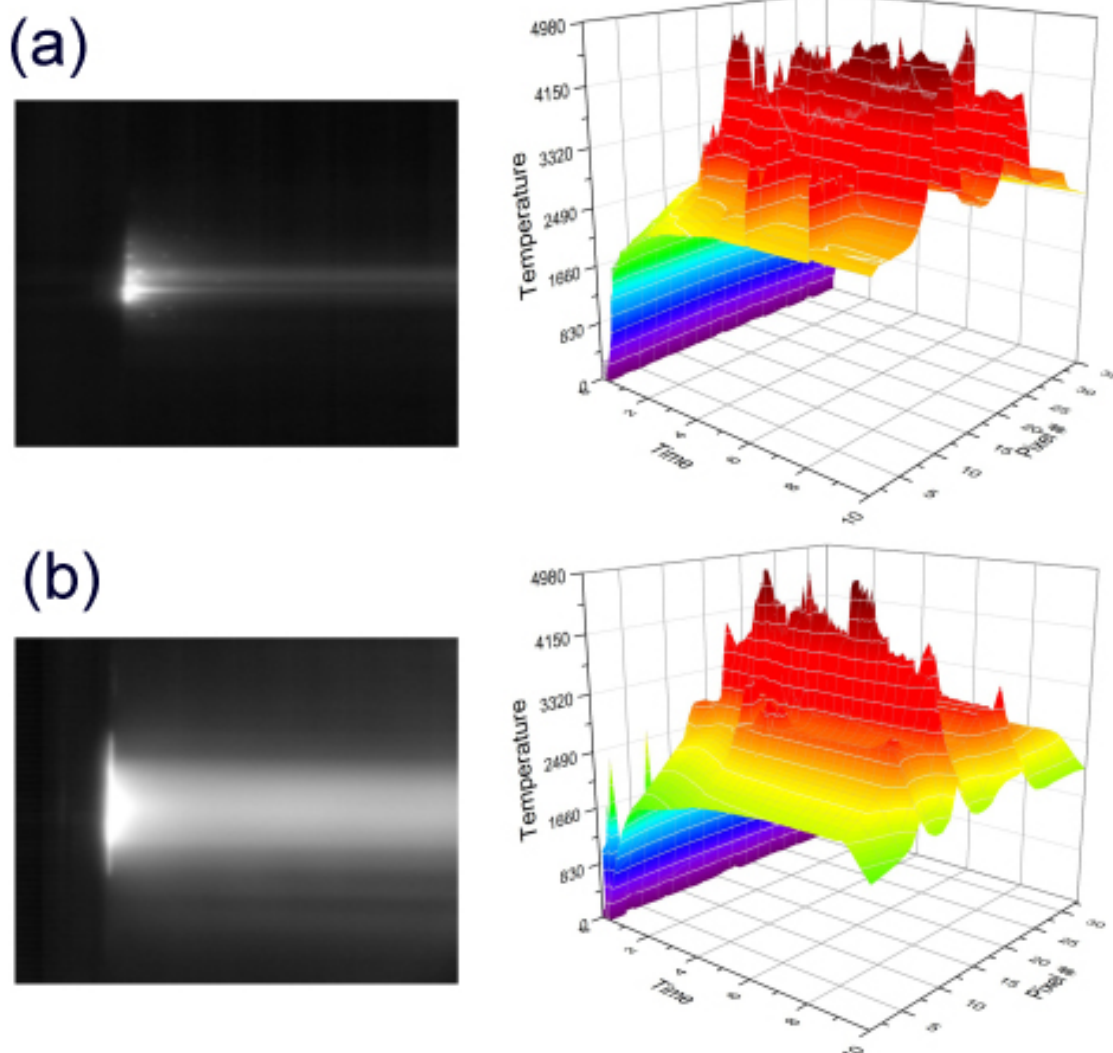
Figure 10. Comparison of a typical fast camera image and evolution of the temperature profile of tungsten during melting induced by (a) helium discharges (1,2 T, 200A) and (b) hydrogen discharges (1.6 T, 220A). To match the plasma-deposited power, the plasma source and magnetic field had to be altered.

that the voids created by helium irradiation promote the formation of bubbles and the ejection of droplets through boiling. It would then imply that droplet ejection should also occur during hydrogen plasmas but the droplets could be too small to be detected by the fast camera imaging.

5. Structure of the re-solidified material

The structure of the re-solidified material was studies by Scanning Electron Microscopy. Fig. 11 shows a photograph of the tungsten surface after melting in Pilot-PSI. It evidences the formation of a hole in the region of the highest heat flux and the accumulation of the re-solidified material around that area, as was described previously.
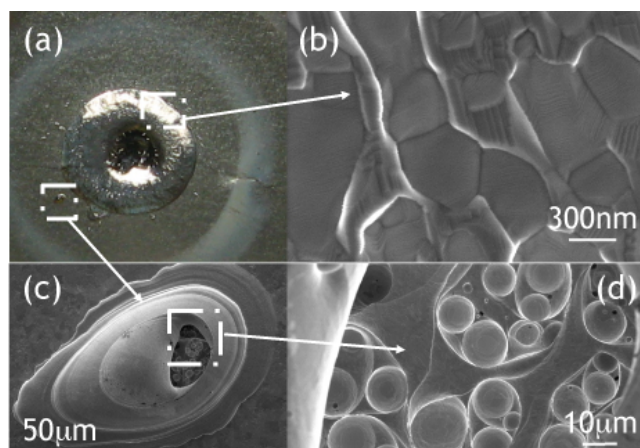
Figure 11. (a) View of a tungsten target after melting. SEM images of (b) the resolidified metal, (c) an elongated droplet observed on the target surface and (c) a zoom into the droplet internal structure.

The structure of the re-solidified material is shown in fig. 11b. The observed morphology is quite similar to typical dendritic structures observed during fast quenching of metallic materials [30] and is characterized by the presence of striations and small grains of irregular shape and size. Around the large pool of molten metal, droplets of different shapes can be observed: either circular droplets or elongated structures such as that shown in fig. 11c. More surprizing is that most of those elongated droplets seem to contain a large number of circular droplets and is shown in f11b and c. Another example of such a structure is shown in fig. 12. Such structures have not been reported before and their formation mechanism is currently not clarified. It is interesting to note that the elongated direction corresponds with the radial direction i.e. is perpendicular to the rotation axis of the molten metal. Since those droplets are observed around the large pool of re-solidified material, it is likely that they have been ejected from the rotating liquid metal. Their internal structure might then be related to boiling.

6. Conclusions

The ability to produce high plasma and heat flux densities in Pilot-PSI, allowed the melting behaviour of aluminium and tungsten to be studied under ITER-divertor relevant plasma conditions. The large applied magnetic field (up to 1.6 T) induces cross-field currents in the plasma which in turn induces rotation of the molten material. Both a rotation and a radial outwards motion are observed with the liquid metal accumulating outside of the area of highest heat flux. This leads to the formation of a hole in the plasma exposed target. The observed dependence on magnetic field strength and target current is compatible with $J \times B$ forces causing the melt-layer rotation.

Statistical analysis of the characteristics of droplet ejection during melting shows that the droplets are mainly ejected in the axial direction with only few particles
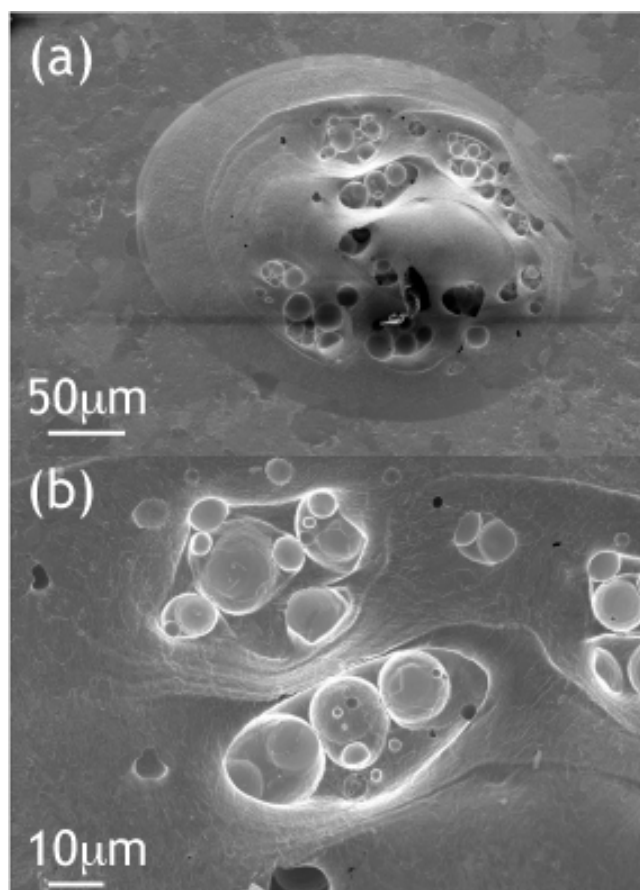
Figure 12. SEM images of (a) an elongated metal droplet and (b) its internal structure.

being ejected with angles higher than 40 degrees. A slight asymmetry of the angular distribution of the ejected droplet appears caused by the gravitational force. The large number of ejected droplets ($\geq$1000) and their relatively high velocities, average 60 m·s^{-1} and up to 160 m·s^{-1} for tungsten, represents a strong source of impurities for the core plasma of a future fusion reactor. On the other hand, the apparent absence of droplet ejection during hydrogen discharges will require further studies to assess its significance for future fusion devices.

7. Acknowledgments

the framework of the EFDA Task Force on Plasma-Wall Interactions. The views and opinions herein do not necessarily reflect those of the European Commission.

References

[1] Pitts R.A., Carpentier S., Escourbiac F., Hirai T., Komarov V., Kukushkin A.S., Lisgo S., Loarte A., Merola M., Mitteau R., Raffray A.R., Shimada M., and Stangeby P.C., 2011 J. Nucl. Mater., 415 S957

[2] Roth J. et al, 2009 J. Nucl. Mater. 390-391 1

[3] Doerner R.P. et al, 2009 Nucl. Fusion 49 035002

[4] De Temmerman G. and Doerner R.P., 2009 J. Nucl. Mater. 389 479

[5] Neu R.L. 2010 IEEE Trans. Plasma Sci. 38 453

[6] Coenen J.W., Philipps V., Brezinsek S., Bazylev B., Kreter A., Hirai T., Laengner M., Tanabe T., Ueda Y., Samm U. and the TEXTOR Team, Nucl. Fusion 51 (2011) 083008

[7] Krieger K., Lunt T., Dux R., Janzer A., Müller H.W., Potzel S., Pütterich T, Yang Z., and the ASDEX Upgrade team, Phys. Scr. T145 (2011) 014067

[8] Garkusha I.E., Makhlaj V.A., Chebotarev V.V., Landman I., Tereshin V.I., Aksenov N.N., and Bandura A.N., J. Nucl. Mater. 390-391 (2009) 814

[9] Litunovsky V.N., Kuznetsov V.E., Lyublin B.V., Ovchinnikov I.B., Titov V.A., and Hassanein A., Fus. Eng. Des., 49-50 (2000) 249

[10] Linke J. 2008 Fusion Sci. Technol. 53 278

[11] De Temmerman G., Bacharis M., Dowling J., and Lisgo S., 2010 Nuclear Fus. 50 105012

[12] Bacharis M., Coppins M., Fundamenski W., and Allen J.E., 2012 Plasma Phys. Control. Fusion 54 085010

[13] Lipschultz B., et al, 2012 Nucl. Fusion 52 123002

[14] De Temmerman G., Zielinski J.J., van Diepen S., Marot L., and Price M., 2011 Nucl. Fusion 51 073008

[15] van der Meiden H.J., Al R.S., Barth C. J., Donne A.J.H., Engeln R., Goedheer W.J., de Groot B., Kleyn A.W., Koppers W.R., Lopes Cardozo N.J., van de Pol M.J., Prins P.R., Schram D.C., Shumack A.E., Smeets P.H.M., Vijvers W.A.J., Westerhout J., Wright G.M., and van Rooij G.J. 2008 *Rev. Sci. Instrum.* 79 013505

[16] G. Sergienko, Priv. Commun.

[17] Roberts S. 1959 Phys. Rev. 114 104

[18] Pitts R.A., 2012 J. Nucl. Mater., in press

[19] Gilligan J., Hahn D., and Mohanti R., 1989 J. Nucl. Mater. 162-164 957

[20] Jaworski M.A. et al 2010 Phys. Rev. Lett. 104 094503

[21] Bazylev B., Igitkhanov Y., Coenen J.W., Philipps V., and Ueda Y. 2011 Phys. Scr. T145 014054

[22] Whyte D., et al, 2004 Fus. Eng. Des. 72 133

[23] Shumack A E, Veremiyenko V P, Schram D C, de Blank H J, Goedheer W J, van der Meiden H J, Vijvers W A J, Westerhout J, Lopes Cardozo N J, van Rooij G J 2008 Phys. Rev. E 78 p 046405

[24] Hong S.H., Grisolia C., and Monier-Garbet P., 2009 Plasma Phys. Contr. Fusion, 51 075013

[25] Bazylev B., Janeschitz G., Landman I., Loarte A., Klimov N.S., Podkovyrovd V.L., and Safronov V.M., 2009 Fus. Eng. Des. 84 441

[26] Miloshevsky G.V., Hassanein A., 2010 Nucl. Fusion 50 115005

[27] Shi Y., Miloshevsky G.V., Hassanein A., 2011 Fus. Eng. Des. 86 155

[28] Ohno N, Ezumi N, Takamura S, Krasheninnikov S I, Pigarov A Yu 1999 Phys. Rev. Lett. 82 p 2216

[29] De Temmerman G. et al, J. Nucl. Mater., submitted

[30] Martyushev N., 2010 Chem. Met. Alloys 3 197